Jia *et al. Applied Biological Chemistry* (2026) 69:8
https://doi.org/10.1186/s13765-025-01077-8

KSABC
The Korean Society for Applied Biological Chemistry

ARTICLE Open Access

Polysaccharide from *Actinidia arguta* leaves and its anti-aging mechanism using the *Caenorhabditis elegans* model

Xuewei Jia[1], Huijie Xue[1], Xiao Yang[2], Qingdan Yan[1], Yuan Gao[1], Yanchong Qin[1], Tianxiao Li[1], Jun Hu[2*] and Chunping Xu[2*]

Abstract

This study examined the structural features and anti-aging mechanisms of a pectic polysaccharide (AAP) extracted from *Actinidia arguta* leaves. AAP was extracted via three-phase partitioning coupled with ammonium sulfate precipitation and subsequently purified on a DEAE-52 cellulose column. Structural characterization *via* FT-IR, GC–MS, NMR, and SEC-MALLS-RI revealed that AAP is a rhamnogalacturonan I (RG-I)-type pectin, consisting of rhamnose, arabinose, galactose, and galacturonic acid with a molar ratio of 20.1:28.4:14.8:36.7, with a weight-average molecular weight (Mw) of 4.14×10^5 g/mol and a random coil conformation in aqueous solution; the Congo red assay confirmed that it does not possess a stable triple-helical structure. In *Caenorhabditis elegans* models, AAP significantly prolonged lifespan and improved exercise capacity, accompanied by reduced accumulation of lipofuscin and reactive oxygen species. Transcriptome profiling revealed 334 differentially expressed genes (DEGs) in response to AAP treatment, with bioinformatics analysis indicating enrichment in metabolic pathways (e.g., lipid metabolism, amino acid metabolism, one-carbon metabolism), extracellular matrix homeostasis, and innate immunity. The key regulated genes included upregulated *fat-7* (lipid desaturase), *alh-2* (aldehyde dehydrogenase), and collagen-encoding genes (*col-138*, *lon-3*) and immune-related *dod-17*, as well as downregulated *fmo-2* (involved in one-carbon metabolism). Protein–protein interaction (PPI) network analysis revealed that collagen-encoding genes and other genes served as core regulatory nodes; qRT–PCR validated the expression trends of key DEGs, such as fat-7, lon-3, and dod-17, which were consistent with the transcriptomic data. These findings demonstrate that AAP exerts antioxidant and anti-aging effects in *C. elegans* by coordinating multiple pathways, emphasizing its potential as a natural anti-aging ingredient for functional foods or pharmaceuticals.

Keywords *Actinidia arguta*, Polysaccharides, Pectin, Antioxidant, Anti-aging, Transcriptomic analysis

*Correspondence:
Jun Hu
huj@ztri.com.cn
Chunping Xu
c.p.xu@zzuli.edu.cn
[1]College of Tobacco Science and Engineering, Zhengzhou University of Light Industry, Zhengzhou 450000, China
[2]Zhengzhou Tobacco Research Institute of CNTC, Zhengzhou 450000, China

© The Author(s) 2026. **Open Access** This article is licensed under a Creative Commons Attribution 4.0 International License, which permits use, sharing, adaptation, distribution and reproduction in any medium or format, as long as you give appropriate credit to the original author(s) and the source, provide a link to the Creative Commons licence, and indicate if changes were made. The images or other third party material in this article are included in the article's Creative Commons licence, unless indicated otherwise in a credit line to the material. If material is not included in the article's Creative Commons licence and your intended use is not permitted by statutory regulation or exceeds the permitted use, you will need to obtain permission directly from the copyright holder. To view a copy of this licence, visit http://creativecommons.org/licenses/by/4.0/.

Springer

Introduction

Actinidia arguta, a perennial deciduous liana of the genus *Actinidia* in the family *Actinidiaceae*, has garnered increasing attention for its nutrient-rich fruits. Recently, interest in its roots, stems, and leaves as potential medicinal resources has increased [1]. The leaves of *A. arguta* are particularly rich in bioactive compounds such as vitamin C, polysaccharides, polyphenols, terpenoids, and various minerals [2] and have demonstrated significant antioxidant [3], anti-inflammatory [4], antibacterial [5], and hypoglycemic activities [6]. Furthermore, they protect erythrocyte membranes from oxidative damage induced by ultraviolet (UV) radiation. Among these compounds, polysaccharides have garnered considerable interest owing to their distinctive structural characteristics and wide-ranging biological functions, showing promising potential for applications in functional foods and pharmaceuticals. Most research has focused on polysaccharides extracted from fruits, which have strong DPPH radical-scavenging activity and are considered promising natural antioxidants [7]. However, studies on leaf-derived polysaccharides remain limited. During the cultivation and management of *A. arguta*, many leaves and branches are pruned and discarded, leading to substantial resource waste. Thus, the extraction and investigation of polysaccharides from *A. arguta* leaves are of considerable scientific and practical importance.

Excessive generation of reactive oxygen species (ROS) is a critical factor contributing to oxidative stress and cellular senescence. This phenomenon is further associated with the development of multiple pathological conditions, such as immune dysfunction and rheumatoid arthritis [8]. Owing to their low toxicity and potent antioxidant properties, natural polysaccharides have emerged as promising antioxidants and anti-aging agents [9]. Research has indicated that polysaccharides can mitigate oxidative damage and delay aging by increasing the activity of antioxidant enzymes [10, 11]. Moreover, they may exert synergistic anti-aging effects through multiple pathways, including inhibition of the *p53*/*p21* senescence signaling pathway, immune system modulation, and maintenance of telomerase activity [12].

Accordingly, this study was designed to extract and isolate a pectic polysaccharide (AAP) from *A. arguta* leaves *via* a three-phase partitioning (TPP) method combined with ammonium sulfate precipitation. The chemical structure of the isolated polysaccharide will be characterized, and its antioxidant and *anti-aging* activities will be evaluated using a *Caenorhabditis elegans* nematode model. This research provides both theoretical insight and a practical foundation for the development of novel natural anti-aging products.

Materials and methods

Materials

All chemicals employed in this research, including KBr, NaH, NaCl, NaClO, NaOH, $NaBH_4$, H_2O_2, acetone, ethanol, trifluoroacetic acid (TFA), t-butanol, acetic anhydride, ammonium sulfate ($(NH_4)_2SO_4$), 1-phenyl-3-methyl-5-pyrazolone (PMP), and 5-fluoro-2′-deoxyuridine (FUDR), were of analytical grade and purchased from Shanghai Chemical Reagent Co., China. Monosaccharide standards, including arabinose (Ara), rhamnose (Rha), galactose (Gal), xylose (Xyl), fructose (Fru), glucose (Glc), mannose (Man), galacturonic acid (GalA) and glucuronic acid (GlcA), were produced by Aladdin Co. (Shanghai, China). DEAE-52 cellulose was obtained from Whatman (Kent, UK). The wild-type *C. elegans* strain N2, *Escherichia coli* OP50, nematode M9 buffer and nematode growth medium (NGM) agar were supplied by SunyBiotech (Fuzhou, China), while the ROS detection kit was obtained from Beyotime Biotechnology (Shanghai, China). All experiments utilized deionized water produced by a Millipore system (USA).

Preparation of AAP

Fresh *A. arguta* leaves were collected from Jilin Province, China, during agronomic pruning in May 2024. The leaves were air-dried in a cool, well-ventilated area prior to use. AAP was extracted and isolated via the TPP method, as previously described [13]. Briefly, 1.0 kg of dried *A. arguta* leaves was chopped into small pieces and homogenized with 1000 mL of distilled water via a laboratory food processor at room temperature (25 °C). Centrifugation of the homogenate at 4000 × g yielded the supernatant. $(NH_4)_2SO_4$ was added to the supernatant at 20% (w/w) and stirred until fully dissolved. The resulting mixture was combined with 1.5 volumes of t-butanol (v/v) and stirred at 35 °C for 30 min. Next, the mixture was subjected to a second centrifugation at 4000 × g for 15 min. The lower aqueous phase was recovered and decolorized *via* hydrogen peroxide treatment. Specifically, the pH was adjusted to 8.0 with 6 mol/L NaOH, hydrogen peroxide was added to a concentration of 15% (v/v), and the reaction proceeded at 50 °C for 60 min. The concentrate was supplemented with ethanol (95%, v/v) to a final concentration of 50% (v/v). The solution was stored at 4 °C for 12 h. Subsequent to centrifugation (4000 × g, 15 min), the resulting precipitate was subsequently redissolved, dialyzed, and lyophilized, yielding the crude polysaccharide.

The crude polysaccharide solution (10 mg/mL in 0.9% NaCl) was applied onto a DEAE-52 cellulose column (4.5 × 100 cm). Stepwise elution was performed with 0, 0.2, 0.4, 0.6, and 0.8 mol/L NaCl at a flow rate of 3.0 mL/min, and 6 mL fractions were collected per tube. The total sugar content was determined via the phenol–sulfuric

acid method, and the absorbance was recorded at 490 nm (Fig. 1). Fractions corresponding to tubes 18–40 were pooled and dialyzed (Mw cutoff = 8 kDa) against deionized water for 72 h. The resulting solution was subsequently, concentrated and lyophilized to obtain the purified AAP. The total carbohydrate and uronic acid contents were measured via the phenol–sulfuric acid assay and the m-hydroxydiphenyl colorimetric method, respectively [14]. The protein content was determined via an automatic azotometer (SKD5000, Shanghai Peiou, China). The Folin–Ciocalteu method was employed to determine the polyphenol content. The degrees of esterification (DE) and acetylation (DA) were determined via titrimetric and hydroxylamine–ferric trichloride assays, respectively [15].

Chemical analysis

Fourier *transform infrared spectroscopy* (FT-IR) of AAP was performed on a Nicolet 5700 spectrometer (Thermo Nicolet Co., USA) via the KBr pellet method, with data collected over the spectral range of 4000–500 cm^{-1}.

The monosaccharide composition of AAP was determined through PMP derivatization prior to chromatography. In brief, AAP was subjected to hydrolysis with 3 M TFA at 110 °C for 6 h in a sealed ampoule. The resulting hydrolysate, along with monosaccharide standards (1 mg/mL), was dissolved in 0.6 M NaOH, combined with an equal volume of 0.5 M PMP in methanol, and heated at 70 °C for 1.5 h. The reaction was halted by adding 0.3 M HCl, and the derivatives were subsequently extracted with chloroform. The monosaccharide composition was examined via a Waters 1525 HPLC system equipped with an Agilent Eclipse XDB-C18 column (5 μm, 4.6 × 250 mm). The analysis was performed at 25 °C with a constant flow rate of 1.0 mL/min. The elution utilized a mobile phase comprising 0.05 M phosphate buffer (pH 7.4) and acetonitrile at a 90:10 (v/v) ratio.

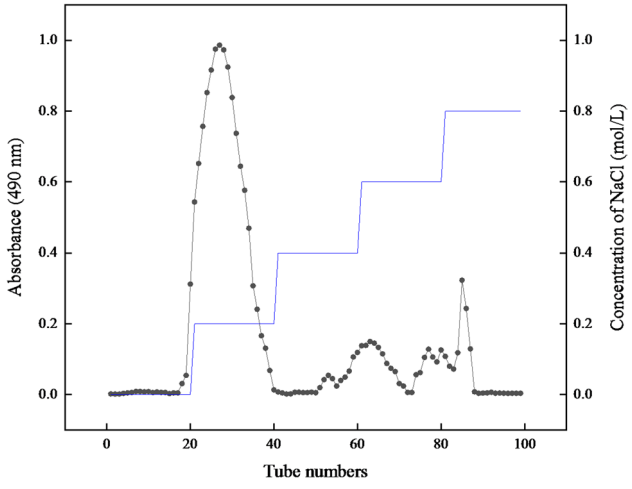


Fig. 1 Elution profiles of AAP on a DEAE-52 column

Methylation analysis was used to detect and analyze the glycosidic bond types of AAP. AAP contains uronic acid, so acidic sugars should be reduced to neutral sugars before methylation analysis. First, 10 mg of AAP was reduced by carbodiimide and sodium borohydride. The methylation reagent (SMSM) was synthesized through the dissolution of 2.5 g NaH in 25 mL of anhydrous DMSO under a nitrogen atmosphere. The reduced AAP underwent triple permethylation using CH_3I in the SMSM, followed by dialysis against deionized water and subsequent freeze-drying. The methylated polysaccharide underwent hydrolysis with 2 M TFA at 120 °C for 6 h, yielding partially methylated monosaccharides, which were then reduced via $NaBH_4$. After drying under a mild nitrogen stream, the residue was dissolved in $CHCl_3$ and neutralized with acetic acid. Subsequently, acetylation was carried out using acetic anhydride at 120 °C for 3 h. The sample was evaporated to dryness under N_2, redissolved in $CHCl_3$, passed through a 0.22 μm membrane filter, and analyzed via gas chromatography–mass spectrometry (GC–MS) (QP2050, Shimadzu, Japan). The samples were separated with a Supelco DB-5 MS chromatographic column (60 m × 0.25 mm *i.d.* × 0.25 μm *d.f.*; Agilent, USA). The carrier gas was high-purity helium with a flow rate of 1.0 mL/min. The column temperature program was as follows: starting at 130 °C, followed by a ramp to 230 °C at a rate of 3 °C/min, maintaining for 5 min. Electron ionization (EI) was performed at 70 eV during mass spectrometric analysis, and the electron multiplier voltage was 1635 V. The mass scanning range was 30–400 amu. The ion source temperature was 230 °C, and a 1.0 μL injection volume was used under splitless conditions.

The structural characterization of AAP was performed via NMR spectroscopy. The ^{1}H NMR, ^{13}C NMR, COSY, HSQC, and HMBC spectra of AAP were obtained on a 600 MHz NMR spectrometer (Avance III, Bruker, Germany) equipped with a standard 5 mm probe. All measurements were conducted at 30 °C using D_2O as the solvent. The polysaccharide concentration was set at approximately 2% (w/w).

Molecular weight (Mw) and chain conformation

The Mw and chain conformation of AAP were analyzed via size exclusion chromatography (SEC) with SB-806 M HQ columns (Showa Denko, Japan) coupled with a multiangle laser light scattering (MALLS) detector (DAWN HELLEOS, λ = 663.7 nm, Wyatt Technology, USA) and a refractive index (RI) detector (Optilab T-rEX, λ = 658.0 nm, Wyatt Technology, USA). The samples were prepared by dissolving them in 0.9% NaCl containing 0.02% sodium azide at 25 °C, followed by filtration

through a 0.22 μm Millipore membrane. The injection volume was 100 μL, the sample concentration was 5 mg/mL, and the mobile phase was delivered at a flow rate of 0.3 mL/min. The refractive index increment (dn/dc) was set at 0.13 mL/g for the molecular weight calculations. Data collection and processing were carried out with Astra software (Version 6.1, Wyatt Technology, USA).

Determination of the triple helix structure

The triple-helical conformation of polysaccharides was investigated via the Congo red assay. Briefly, 1 mL of polysaccharide mixture (1 mg/mL) was mixed with an equal volume of Congo red solution (100 μmol/L). A 1 mol/L NaOH solution was subsequently gradually added to the mixture to achieve final NaOH concentrations ranging from 0 to 0.5 mol/L (in increments of 0.1 mol/L). The mixtures were equilibrated for 10 min at room temperature. The maximum absorption wavelength (λmax) within the range of 400–700 nm was recorded via a UV−Vis spectrophotometer. A blank control was set up by replacing the polysaccharide solution with deionized water.

Maintenance and synchronization of *C. elegans* strains

C. elegans were maintained on NGM plates coated with *E. coli* OP50 and incubated at 20 °C in a biochemical incubator. For synchronization, adult nematodes were washed with M9 buffer and lysed with bleaching solution containing NaClO and NaOH. The resulting eggs were collected, centrifuged, washed, and incubated overnight in M9 buffer to obtain L1 larvae, which were subsequently cultured at 20 °C for 48 h to reach the L4 stage.

Effects of AAP on the lifespan and exercise capacity of *C. elegans*

AAP at different concentrations was incorporated into NGM plates supplemented with 50 mmol/L FUDR. Approximately 30 synchronized L4-stage nematodes were randomly selected and transferred to each plate, with three replicate plates per group. Nematodes were transferred to fresh AAP-containing plates every 48 h to prevent progeny interference. Survival was assessed daily; nematodes were considered nonviable and subsequently excluded from analysis if they exhibited no reaction when a platinum wire was gently prodded for mechanical stimulation. This process continued until all the nematodes had perished.

To assess exercise capacity, body bending frequency was measured on days 1, 3, 6, and 9by counting the number of body bends of a single nematode within 30 s. AAP treatments were administered starting from the L4 stage and continued until death. The AAP concentrations used were 50 μg/mL (L-AAP), 100 μg/mL (M-AAP), and 500 μg/mL (H-AAP). Throughout the experiment, treated nematodes were transferred to fresh NGM plates bidaily to ensure experimental consistency.

Determination of Lipofuscin and ROS accumulation

After 10 days of culture, L4-synchronized nematodes were rinsed three times with M9 buffer and subsequently placed onto 2% agar pads. Two drops of 0.2% sodium azide were applied to immobilize the nematodes. Lipofuscin autofluorescence was captured via a fluorescence microscope (MF53-N, Mshot, China), and the fluorescence intensity was quantified via ImageJ software.

Intracellular reactive oxygen species (ROS) levels were measured with the fluorescent probe 2′,7′-dichlorodihydrofluorescein diacetate (H_2DCF-DA). L4-synchronized nematodes were cultured on AAP- and/or 2% glucose-supplemented NGM plates containing FUDR then transferred to FUDR-free plates and incubated at 20 °C for 5 days. After collection and rinsing with M9 buffer, nematodes were transferred to 24-well plates containing 50 μM H_2DCF-DA and incubated in the dark at 20 °C for 1 h. After repeated washes to remove excess dye, the nematodes were mounted on agarose pads and imaged under a fluorescence microscope for ROS detection.

Transcriptomic analysis

Total RNA was extracted from synchronized *C. elegans* after 48 h of culture via the TRIzol method. Two groups including three biological replicates were analyzed: the control group (K1, K2, and K3) and the treatment groups (T1, T2, and T3) exposed to 0.2 mg/mL AAP. Genomic DNA was removed via DNase I. RNA quality was evaluated via the Agilent 2100 Bioanalyzer system (Agilent Technologies). Each RNA sample was extracted from more than 500 nematodes. RNA-seq libraries were prepared and profiled via high-throughput sequencing on the Illumina platform. The raw sequencing data were subjected to quality control to obtain clean data for downstream analyses. High-quality sequencing reads were mapped to the reference genome via the HISAT2 alignment tool (http://ccb.jhu.edu/software/hisat2/index.shtml), and the resulting alignment files served as the basis for subsequent transcript assembly and expression-level quantification. The quality assessment of the sequencing alignment included evaluations of sequencing saturation, gene coverage, read distribution across genomic regions, and chromosomal distribution. Gene expression levels were calculated on the basis of read counts mapped to genomic regions. Differentially expressed genes (DEGs) were detected through DESeq2 on the basis of read count data aligned to genes. The screening criteria were set as a false discovery rate (FDR) < 0.05 and a |log2-fold change (FC)| ≥ 1. Kyoto Encyclopaedia of Genes and Genomes (KEGG) pathway enrichment analysis was conducted with the KOBAS platform (http://kobas.cbi.pku.edu.cn/).

Table 1 Monosaccharide composition of AAP

Item	AAP
Chemical composition (%, w/w)	
Total carbohydrate	97.2
Uronic acid	37.3
Protein	0.87
Phenol	nd
Monosaccharide composition (mol %)	
Rha	20.1
Ara	28.4
Gal	14.8
GalA	36.7
DA	6.2
DE	14.6

nd: Not detected

Table 2 Results of the methylation analysis of AAP

Methylated sugar	Linkage type	Molar ratio
2,3,5-Me_3-Ara*p*	α-Ara-(1→	17.9
2,3-Me_2-Ara*p*	→5)-α-Ara-(1→	7.2
3,4-Me_2-Rha*p*	→2)-α-D-Rha-(1→	5.5
3-Me-Rha*p*	→2,4)-α-D-Rha-(1→	16.4
2,4,6-Me_3-Gal*p*	→3)-β-D-Gal-(1→	15.1
2,3,6-Me_3-Gal*p*	→4)-α-D-GalA-(1→	31.5
3,6-Me_2-Gal*p*	→4)−2-OAc-α-D-GalA-(1→	1.9
2,3-Me_2-Gal*p*	→4)-α-D-GalA-6-OMe-(1→	4.5

qRT–PCR validation

To validate the transcriptome sequencing results, five differentially expressed genes were analyzed via quantitative real-time PCR (qRT−PCR). Nematode samples from the control and AAP-treated groups were collected. Total RNA was extracted via TRIzol reagent, and its concentration and purity were measured with a NanoDrop spectrophotometer. Genomic DNA was removed via DNase I, and reverse transcription was performed via the TranscriPtor cDNA Synth Kit. qPCR amplification was performed via SYBR Green chemistry with 2× Color SYBR Green qPCR Master Mix (ROX1 plus). The thermal cycling conditions were as follows: initial denaturation at 95 °C for 5 min, followed by 40 cycles of 95 °C for 10 s and 60 °C for 30 s. The experiment included three independent biological replicates.

The *Caenorhabditis elegans act-1* gene served as the internal reference. Relative gene expression was calculated via the $2^{-\Delta\Delta CT}$ method. All primer sequences are listed in Table 1.

Statistical analysis

All the experiments were repeated at least three times to ensure reproducibility. The results are presented as X ± SD. Statistical analysis was performed via Origin 2021 software, and differences were considered statistically significant at $p < 0.05$.

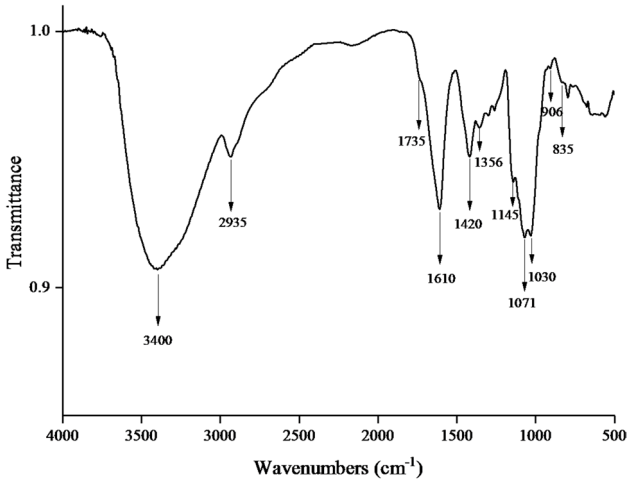


Fig. 2 FT-IR spectra of AAP

Results and discussion

Chemical analysis

The yield of crude polysaccharide was 7.03%, and further purification with DEAE-cellulose 52 resulted in the isolation of AAP, with a recovery rate of 64.8%. As shown in Table 2, AAP was found to contain 97.2% total carbohydrates and 37.3% uronic acids, indicating that it is an acidic pectic polysaccharide. The protein content, calculated from the nitrogen content, was 0.87%, and no phenolic compounds were detected. Monosaccharide composition analysis revealed that AAP was primarily composed of Rha, Ara, Gal, and GalA at molar ratios of 20.1:28.4:14.8:36.7, respectively. Pectin consists mainly of galacturonic acid-based linear polysaccharide chains, with GalA residues often esterified by functional groups such as methoxyl or amide groups. The DE and DA for AAP were 6.2 and 14.6, respectively, indicating a relatively low level of esterification.

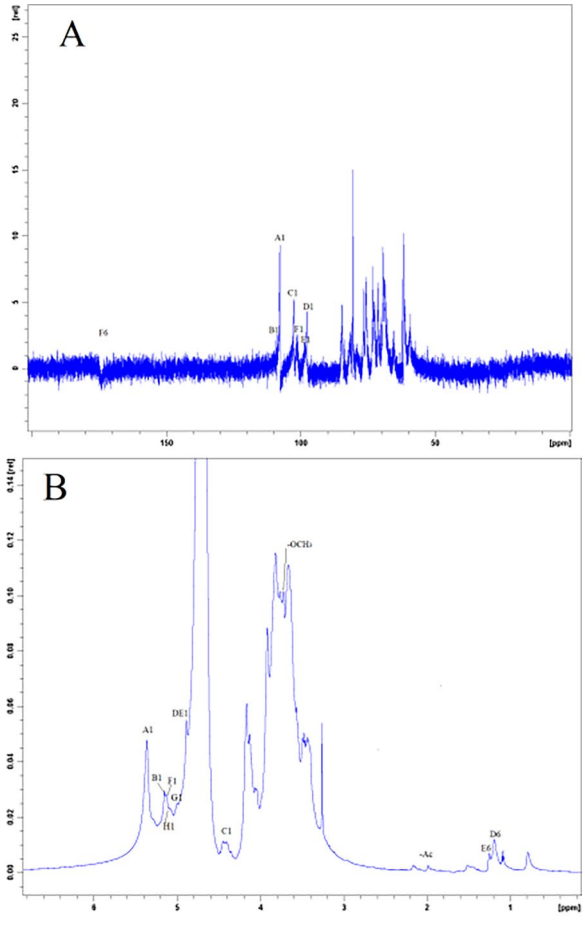
Pectins are composed of four different structures: linear homogalacturonan (HG), branched rhamnogalacturonan (RG-I and RG-II) and xylogalacturonan (XG), which collectively define the "smooth" (HG) and "hairy" (RG-I, RG-II) regions of pectin [16]. The RG-I backbone consists of repeating disaccharide units of Rha and GalA. The HG and RG-II domains are composed primarily of polygalacturonic acid chains linked *via* α−1,4-glycosidic bonds, whereas substitution at the O-3 or O-4 position of GalA by xylose results in the XG structure [17]. Pectin is classified mainly as RG-I when the Rha/GalA molar ratio ranges from 0.05 to 1.00. In contrast, a ratio less than 0.05 suggests an HG- or RG-II-type structure. The Rha/GalA molar ratio in AAP was determined to be 0.55, suggesting that AAP predominantly consists of an RG-I-type pectin structure.

The structural properties of AAP were analyzed in greater depth via FT-IR, GC−MS, and NMR spectroscopy. Figure 2 shows the FT-IR spectrum of AAP. The

Table 3 Summary of the ^{1}H and ^{13}C chemical shifts of AAP

Residue		Chemical shifts (ppm)							
		1	2	3	4	5	6	CH_3O	CH_3CO
α-Ara-(1→	H	5.35	4.17	3.93	4.06	3.62, 3.72			
(A)	C	107.7	84.8	75.6	84.5	61.3			
→5)-α-Ara-(1→	H	5.15	4.13	3.94	4.03	3.66, 3.90			
(B)	C	109.2	84.4	75.6	83.8	65.4			
→3)-β-D-Gal-(1→ (C)	H	4.45	3.42	3.82	3.64	3.90	3.47, 3.55		
	C	102.9	69.4	81.8	71.3	80.7	62.4		
→2,4)-α-D-Rha-(1→ (D)	H	4.89	4.04	3.82	4.17	3.92	1.20		
	C	97.9	83.8	70.0	84.9	68.4	22.8		
→2)-α-D-Rha-(1→ (E)	H	4.89	nd	nd	nd	3.96	1.25		
	C	98.5	nd	nd	nd	69.2	19.7		
→4)-α-D-GalA-(1→ (F)	H	5.13	3.62	3.85	3.48	4.16			
	C	101.3	73.4	76.4	71.3	80.6	174.1		
→4)–2-OAc-α-D-GalA-(1→ (G)	H	5.01	3.99	nd	nd	nd			1.99
	C	98.75	nd	nd	nd	nd	173.4		20.1
→4) -α-D-GalA-6-OMe-(1→ (H)	H	5.09	nd	nd	nd	nd		3.72	
	C	nd	nd	nd	nd	nd	170.9	52.7	

nd: Not detected or not identified



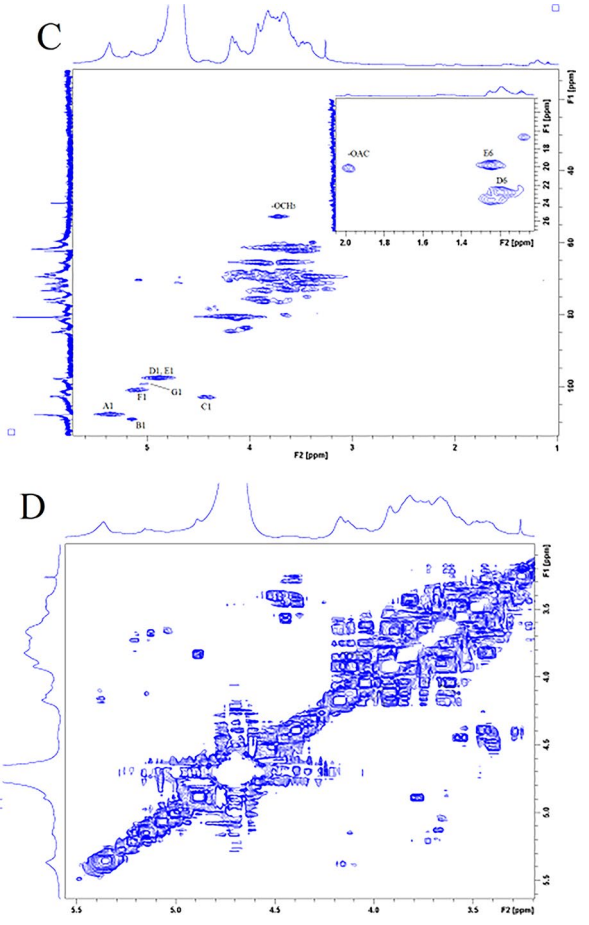


Fig. 3 The ^{13}C NMR (**A**), ^{1}H NMR (**B**), HSQC (**C**), COSY (**D**), and HMBC (**E**) spectra of AAP in D_2O

Fig. 3 (continued)

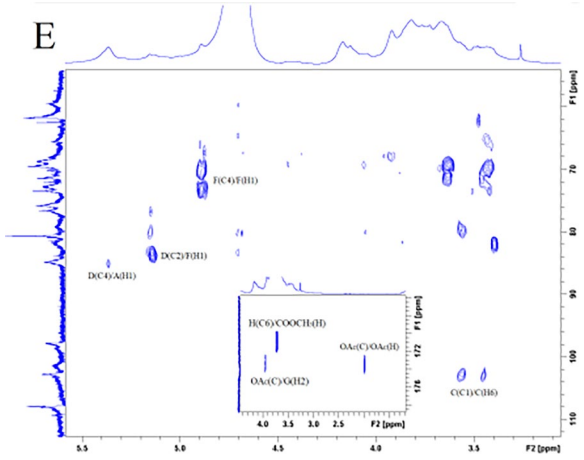


Fig. 3 (continued)

peak detected near 3400 cm^{-1} is associated with O–H stretching, whereas the peak close to 2935 cm^{-1} is linked to C–H bond vibrations. Notably, the esterified carboxyl group (COOR) at 1735 cm^{-1} was present. The absorption peaks near 1610 cm^{-1} and 1420 cm^{-1} are indicative of typical FT-IR spectral features associated with polysaccharides. The peak in the spectral region between 1200 and 1400 cm^{-1} is attributed mainly to C–H deformation vibrations and C–OH bending vibrations. The absorptions at 1030, 1071 and 1145 cm^{-1} are characteristic of sugar ring vibrations [18]. Furthermore, the peak at 835 cm^{-1} indicates the existence of an α-type glycosidic linkage, whereas the weak band at 906 cm^{-1} is indicative of a β-type glycosidic linkage [19].

To determine the linkage patterns of the monosaccharides, AAP was subjected to reduction, permethylation, and subsequent GC–MS analysis. As shown in Tables 3 and 8 partially methylated alditol acetates were characterized. The predominant derivative was 2,3,6-Me3-Gal*p* (31.5%), indicating that ASPP was primarily composed of 1,4-linked GalA residues. This is essentially consistent with the structure of pectin, which is composed of GalA as the main chain mixed with some Rha and Ara as the side chain attached to the Rha residue [20].

Detailed structural information on AAP was obtained through 1D NMR and 2D NMR spectroscopy (Fig. 3). In the ^{13}C, ^{1}H, and HSQC spectra (Fig. 3A, B and C), anomeric proton and carbon signals were observed at 5.35/107.74, 5.15/109.20, 4.45/102.87, 4.89/97.75, 4.89/98.52, 5.13/101.33, and 5.01/98.75 ppm, respectively, which were labeled A-G. Typically, anomeric proton signals of the α- and β-configurations appeared at 4.95–6.0 ppm and 4.4–4.95 ppm, respectively [20]. Therefore, AAP is a heterooligosaccharide with both α- and β-configurations, where residue C is in the β-configuration and the remaining residues are in the α-configuration, showing overall agreement with the FT-IR findings.

The monosaccharide composition and methylation analysis results indicated that AAP contains typical pectin glycans. HG is composed of a straight chain of →4)-α-GalpA-(1→. RG-I possesses a backbone composed of alternating →4)-α-GalpA-(1→ and →2)-α-Rhap-(1→ units, typically decorated with Ara and Gal side chains. The C1 of Ara is in a lower field close to 110 ppm, so residues A and B should be Ara with different linkages[15]. From the COSY spectrum (Fig. 3D), for residue A, the remaining proton signals (H-2 to H-5) were sequentially identified as 4.17, 3.93, 4.06, 3.62, and 3.72 ppm; from the HSQC spectrum, the associated carbon resonances (C-2 to C-5) appeared at 84.77, 75.55, 84.51, and 61.30 ppm, respectively. Residue A was determined to be terminal α-Ara-(1→. Similar signals of residues B and C were sequentially identified and are listed in Table 3. The C5 of residue B shifted to a lower field of 65.35 ppm, indicating →5)-α-Ara-(1→, and the C3 of residue C showed a downfield displacement to 81.78 ppm, indicating →3)-β-D-Gal-(1→. Residues A, B, and C suggest the presence of arabinogalactan, a typical branching structure found in RG-I-type pectin.

Residue D was assigned through its distinct anomeric signals at 4.89/97.85 ppm, and the chemical shifts from H-2/C-2 to H-6/C-6 obtained via COSY and HSQC spectra are provided in Table 4. The resonance signal near 1.20 ppm originated from the methyl group of Rha. Combined with the lower-field signals of C-2 and C-4 at 83.80 ppm and 83.50 ppm, residue D was determined to be →2,4)-α-L-Rhap-(1→, a branching site in the pectin backbone[15]. Similarly, residue E was identified as →2)-α-L-Rhap-(1→. Combined with the monosaccharide composition, the lower-field signal at approximately 174 ppm in the ^{13}C spectrum was attributed to the carboxyl carbon (C-6) of galacturonic acid (GalpA). The lower-field resonance signal of C-4 at 71.34 ppm indicated that residue F was →4)-α-GalpA-(1→. GalA can be partially methyl esterified at C-6 and acetyl esterified at O-2 or O-3. The obvious δ 1.99/20.12 ppm signal in the HSQC spectrum indicated the presence of an acetyl group (OAc), which was corroborated by the cross peak at δ 1.99/173.43 ppm in the HMBC spectrum [21]. In addition, the δ 3.99/173.43 (H-2/OAc) ppm signal in the HMBC spectrum showed that the OAc group was linked to O-2 of GalA. Thus, residue G was identified as →4)–2-O-Ac-α-D-GalpA-(1→. Similarly, the low-content residue H was determined to be →4)-α-D-GalpA-6-OMe-(1→. In contrast to residue G, residue H lacked an acetyl substituent but possessed a methyl ester group, as indicated by the δ 3.72/52.73 peak in the HSQC spectrum and corroborated by the δ 3.72/170.9 correlation in the HMBC spectrum.

Table 4 Experimental results from SEC-RI-MALLS for AAP

Parameters[a]		AAP
Masses	Injected Mass (μg)	492.0
	Calculated Mass (μg)	483.6
	Mass Recovery (%)	98.3
	Mass Fraction (%)	100.0
Molar mass (g/mol)	Mn	1.09×10^5 (± 13.72%)
	Mw	4.14×10^5 (± 1.99%)
Dispersity	Mw/Mn	3.80 (± 13.96%)
RMS radius (nm)	Rn	59.1 (± 15.0%)
	Rw	78.5 (± 1.9%)

Mn and Mw refer to the number- and weight-average molecular weights, respectively. Rn and Rw refer to the number and weight-average square mean radius of gyration, respectively

Table 5 Primer sequences for qRT–PCR

Primer name	Sequences (5′–3′)
act-1-F	TCTGGATCGGAGGATTATTCTATTCT
act-1-R	AAGCACTTTCGTGAACAATC
fat-7-F	CGAGCATTGCCAAGAAGAT
fat-7-R	GCCGTTTGCCATTTAGCA
lon-3-F	TCGGTTGCAGTTTTCGGGTATA
lon-3-R	AACTACAAGCTTCCGGGCTAAA
dod-17-F	ACAGCACAGGACCGACTGGATG
dod-17-R	TACACCAACGCGCTTCTCAACG
K01C8.1-F	TGTCGTATCAGATAGACCAGGAG
K01C8.1-R	CGTGGAATACATCCGTTGAGAT
fmo-2-F	AAGCTGGAGACACGAGGATT
fmo-2-R	GGAGTTAAGCATAGCTTGAGGAA

On the basis of the cross-peaks detected in the HMBC spectrum (Fig. 3E), the glycosidic bond positions and sequence of sugar linkages within the polysaccharide were elucidated. The strong correlation peak between H-1 (5.13 ppm) and C-4 (71.34 ppm) of residue F indicated the presence of →4)-α-GalpA-(1→4)-α-GalpA-(1→). The cross peak at 5.13/83.8 ppm verified the arrangement of →4)-α-GalpA-(1→2)-α-Rhap-(1→. The cross peak at 5.35/84.88 ppm revealed the existence of an α-Ara-(1→4)-α-D-Rha-(1→ linkage. Therefore, integrating all the above results, we infer that AAP may have a pectin structure containing HG and RG-I fragments. Rha, GalA, and their esters constitute the smooth backbone region of pectin, with the branching site being →2,4)-α-L-Rhap-(1→ and Ara and Gal as the main side chains. However, owing to its high Mw and complex structural features, its specific primary structure is difficult to determine.

Mw and chain conformation

The molecular characteristics of AAP were analyzed via SEC-MALLS-RI. The findings are presented in Table 5. The dispersity (Mw/Mn) of AAP was 3.80, indicating a broad molecular weight distribution and poor uniformity.

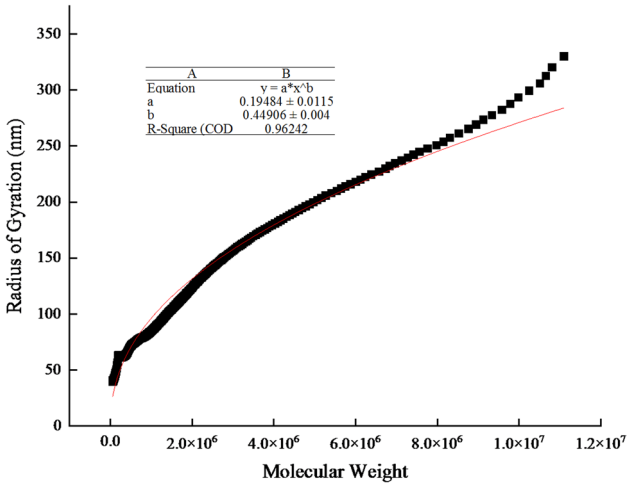


Fig. 4 Plot of Rw vs. Mw for AAP in 0.9% NaCl buffer containing 0.02% sodium azide at 25 °C

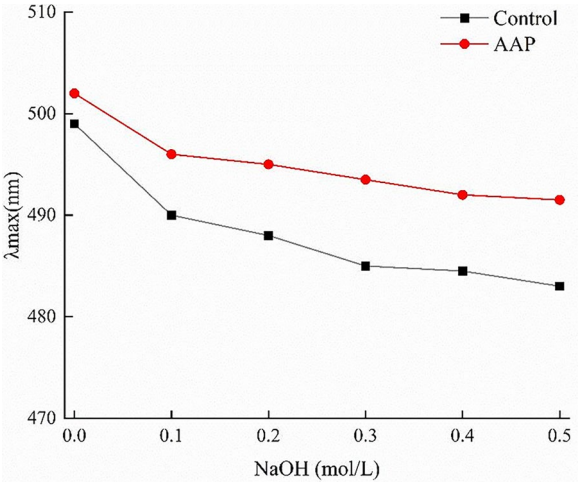


Fig. 5 Congo red assay of AAP

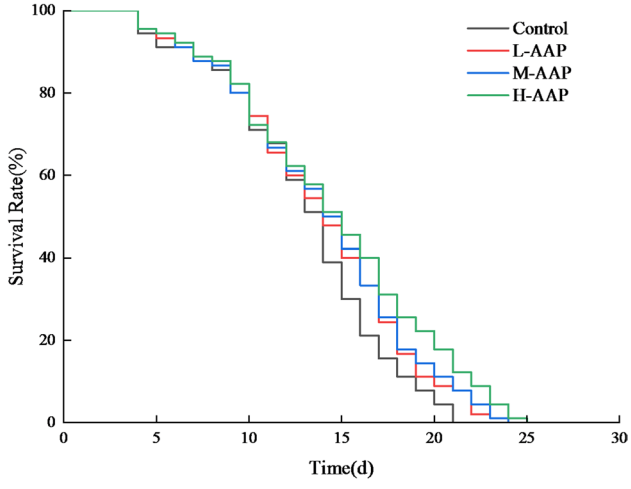


Fig. 6 Effects of AAP on lifespan

This suggests significant heterogeneity in polysaccharide molecular size. The molecular conformation of AAP in aqueous solution was evaluated by plotting the RMS radius (Rw) against Mw via the power-law equation $R_w=kMw^{\alpha}$, where the exponent α provides insight into the spatial conformation of the polymer. As shown in Fig. 4, the curve fitting yielded a correlation coefficient of 0.96, indicating reliable data fitting. The value of α reflects the polymer's chain flexibility in solution [8]. Typically:

α ≈ 0.3 corresponds to a compact globular structure,

α ≈ 0.5 indicates a random coil,

α ≈ 1.0 represents a rigid rod-like structure.

Higher α values denote increased chain stiffness. Linear polysaccharides tend to adopt extended or fibrous conformations because of the free orientation of their repeating segments. In contrast, branched or crosslinked polymers are more prone to forming globular shapes, as branching and crosslinking restrict segmental motion. For AAP, the calculated α value was 0.449, suggesting that it adopts a random coil conformation in aqueous solution. This observation aligns well with its identified structural features, particularly the HG and RG-I backbone.

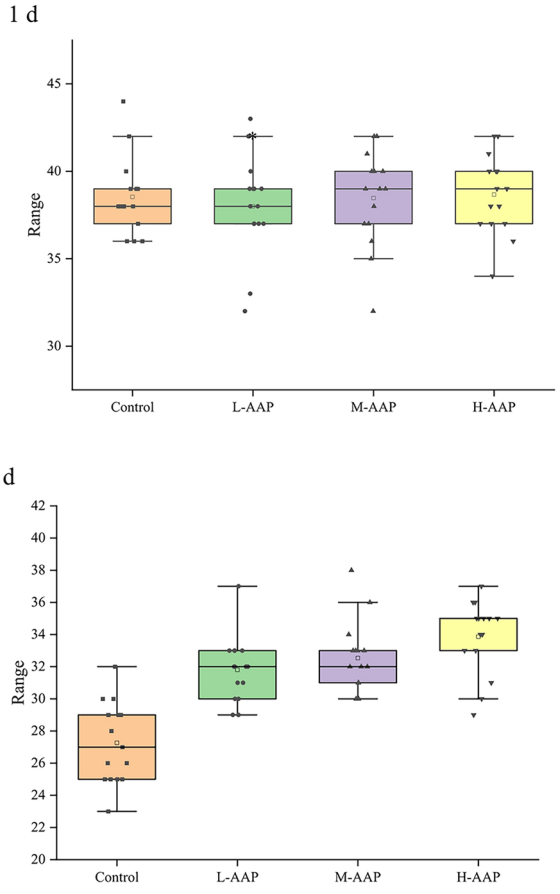


Fig. 7 Effects of AAP on the exercise capacity of *C. elegans*

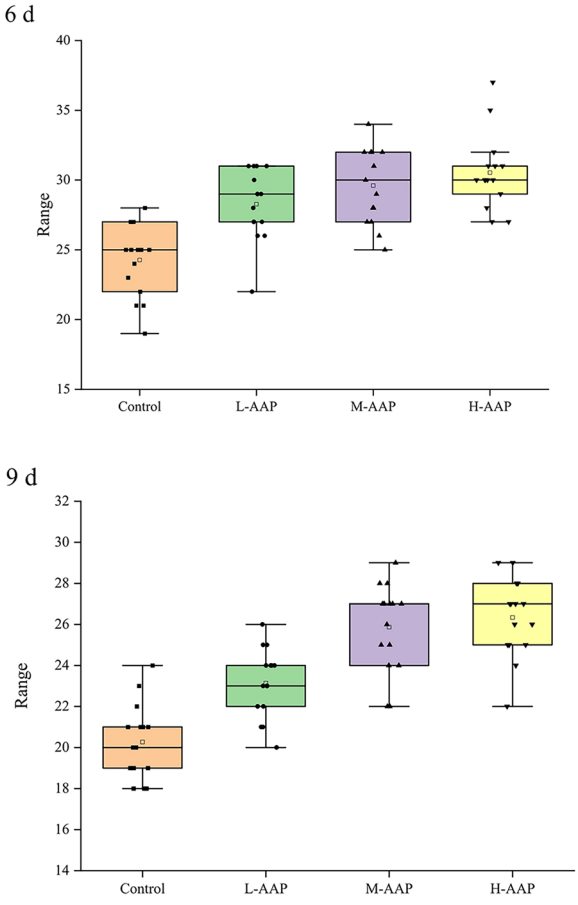


Fig. 7 (continued)

Analysis of the triple helix structure

Congo red specifically binds to polysaccharides with a triple-helical conformation, forming a complex that exhibits a distinct redshift in its maximum absorption wavelength (λmax) under moderately alkaline conditions. However, excessive alkali disrupts the complex, resulting in a decrease in λmax. As shown in Fig. 5, the Congo red assay for AAP polysaccharides demonstrated no such redshift compared with that of the Congo red control. Instead, the λmax decreased progressively with increasing NaOH concentration. This response contrasts sharply with the characteristic behavior of a triple-helix–Congo red complex and indicates that AAP does not adopt a stable triple-helical conformation under the tested conditions.

Effects of AAP on the lifespan and exercise capacity of *C. elegans*

Aging is a progressive, time-related process, and lifespan serves as a direct and informative biological marker for evaluating age-associated changes. First, the influence of varying AAP concentrations on the lifespan of *C. elegans*

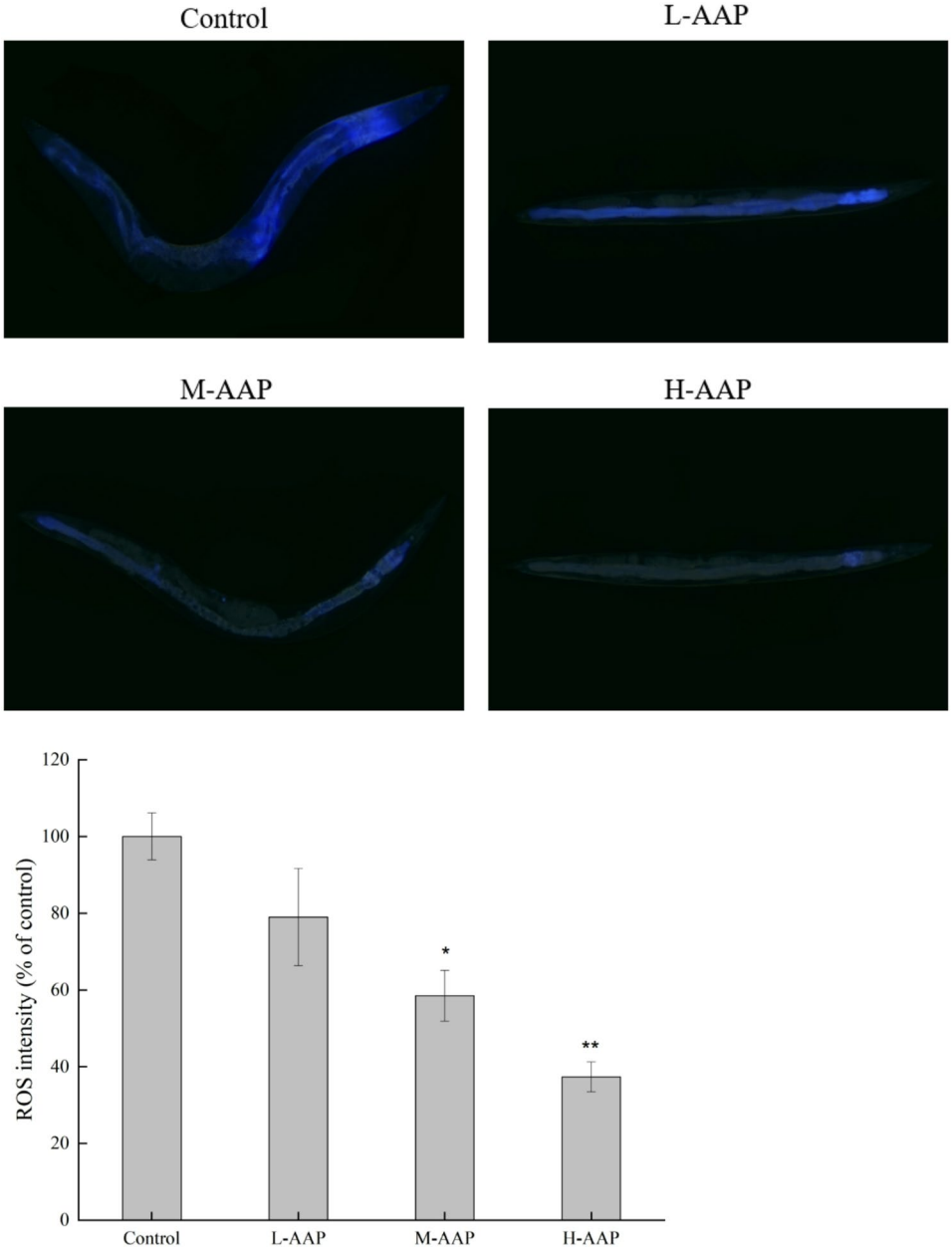


Fig. 8 Typical fluorescence images of lipofuscin accumulation and statistical results of fluorescence intensity ($n = 20$, * $p < 0.05$, ** $p < 0.01$ compared with control nematodes)

(N2) was assessed. Figure 6 shows the survival curves of *C. elegans* at different AAP concentrations. Compared with the control group, the addition of low, medium and high concentrations of AAP to ordinary NGM Petri dishes significantly improved the lifespan of *C. elegans*. The final death times of the insects were 21, 24, 24 and 25 days. The anti-aging effects of AAP were more pronounced in the later stages. After culture for approximately 15 days, the improvement in the administration group was very obvious.

The exercise capacity was characterized by body bending frequency. As shown in Fig. 7, the body bending frequency of nematodes gradually decreased over time, which indicates a decline in exercise capacity during the aging process. This study investigated the effects of various treatments on nematode exercise capacity on days 1, 3, 6, and 9. Although there was no significant difference on the first day, beginning on the third day, compared with those in the control group, the head swing frequency of the nematodes in each treatment group significantly increased. These findings demonstrate that AAP

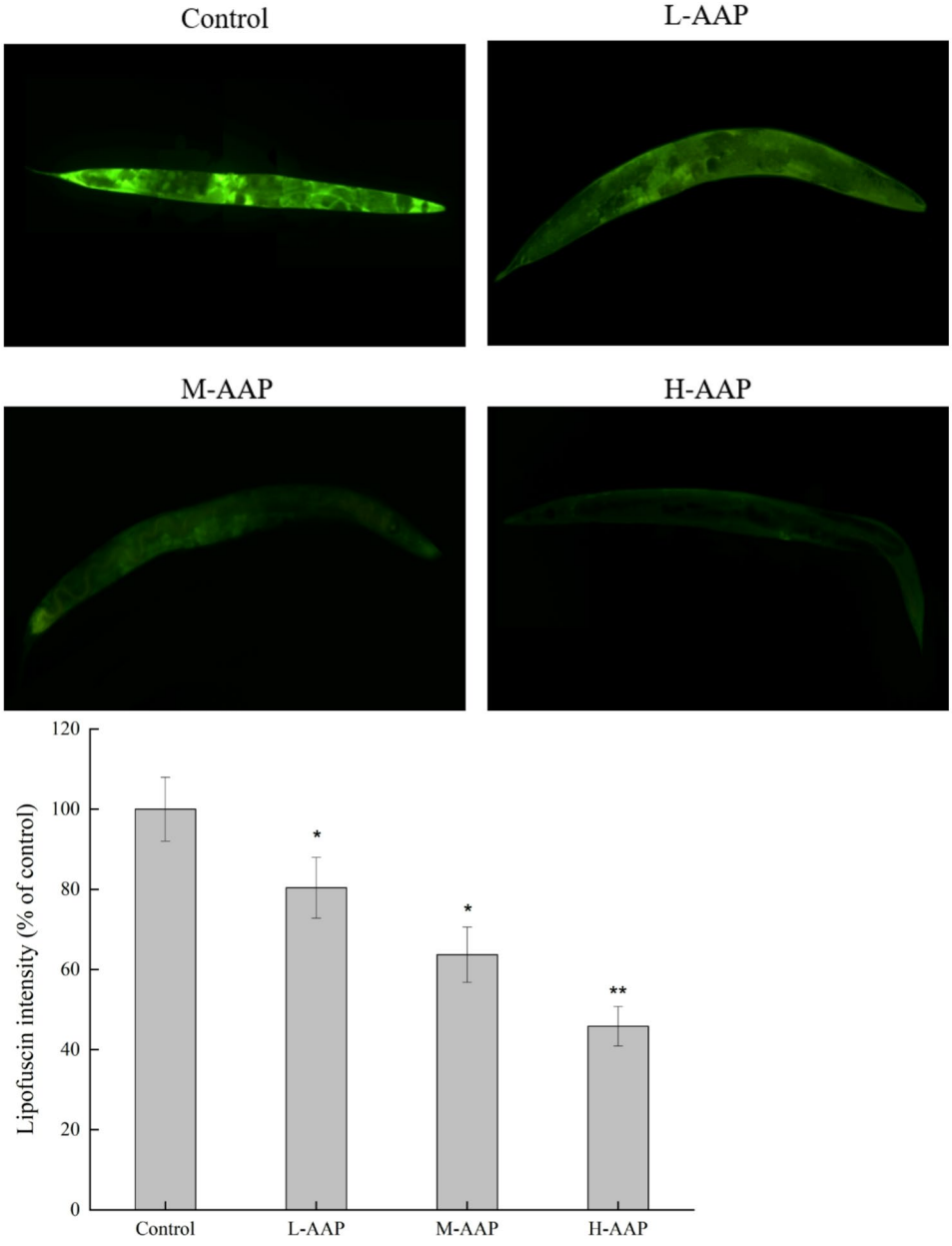


Fig. 9 Typical fluorescence images of ROS accumulation and statistical results of fluorescence intensity ($n = 20$, * $p < 0.05$, ** $p < 0.01$ compared with control nematodes)

can not only prolong the lifespan of nematodes but also increase their exercise capacity.

Effects of AAP on the accumulation of Lipofuscin and ROS

Lipofuscin is an autofluorescent pigment with a characteristic brownish-yellow appearance. As a recognized biomarker of oxidative stress and lipid metabolism disorders [22], lipofuscin accumulation reflects age-associated cellular damage. In this study, the lipofuscin content in *C. elegans* was evaluated after 10 days of AAP treatment. Representative fluorescence images were captured, and the fluorescence intensity was quantified via ImageJ software; more than 20 nematodes per group were analyzed (Fig. 8). AAP treatment led to a dose-dependent reduction in lipofuscin levels: 19.59%, 36.29%, and 54.16% reductions were observed at low, medium, and high concentrations, respectively, indicating a significant anti-aging effect.

Intracellular ROS levels were assessed via the fluorescent probe H_2DCF-DA, which is initially nonfluorescent. After deacetylation by intracellular esterases, it is oxidized by ROS to form the fluorescent compound 2′,7′-dichlorofluorescein (DCF) [23]. Quantitative fluorescence analysis revealed that AAP significantly reduced

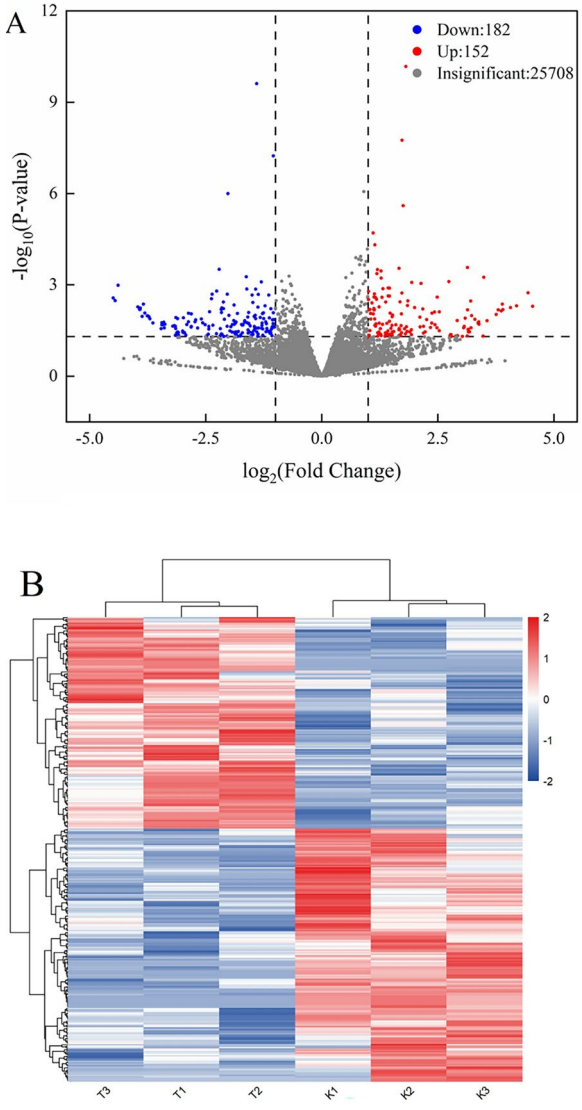


Fig. 10 Volcano plot (**A**) and cluster heatmap (**B**) of DEGs between the control group (K1, K2, K3) and the AAP group (T1, T2, T3)

ROS levels in a concentration-dependent manner, with decreases of 21.01%, 41.51%, and 62.63% at low, medium, and high doses, respectively (Fig. 9). These findings suggest that AAP effectively mitigates oxidative stress in *C. elegans* by reducing intracellular ROS accumulation.

DEG analysis

To clarify the molecular basis of the anti-aging activity of polysaccharides, transcriptomic profiling was conducted at the gene expression level. High-throughput RNA sequencing was conducted via the Illumina platform to systematically evaluate gene expression changes in *C. elegans* following treatment with high-dose AAP (T1, T2, and T3). After quality-control filtering, sequencing data from both the control and AAP-treated groups exhibited high base-calling accuracy, satisfying the Q20 (≥ 95% of bases with a Phred quality score ≥ 20) and Q30 (≥ 90% of bases with a Phred quality score ≥ 30) thresholds. This ensured that the dataset was of sufficient quality for reliable downstream bioinformatics analysis.

A total of 334 DEGs were screened according to the criteria $p < 0.05$ and $|\log_2(\text{fold change})| > 1$. Among these genes, 152 were significantly upregulated and 182 were downregulated in response to H-AAP treatment. Bioinformatic visualization, including a volcano plot (Fig. 10A) and hierarchical clustering heatmap (Fig. 10B), revealed clear segregation between the treatment and control groups, demonstrating both strong biological reproducibility and distinct transcriptomic alterations induced by AAP. These findings confirm the reliability of the sequencing data and imply that the identified DEGs could be crucial for the lifespan regulation of *C. elegans*, providing molecular evidence for the anti-aging effects of AAP.

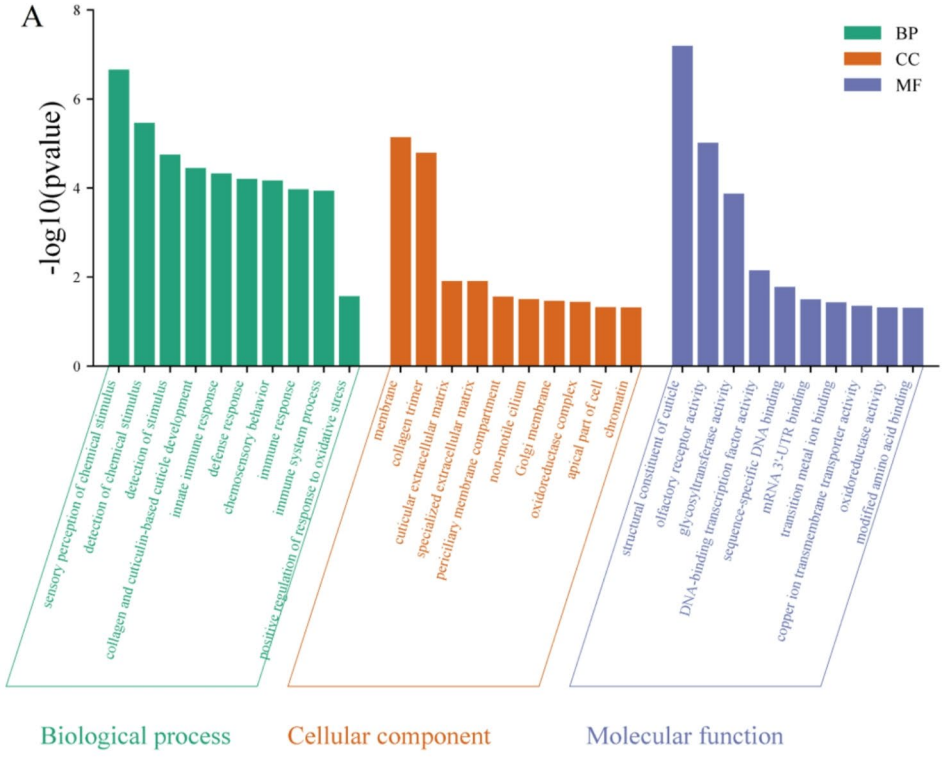
GO enrichment analysis

Gene Ontology (GO) analysis was conducted to annotate the potential functions of the DEGs, which were categorized into three primary domains: biological process, cellular component, and molecular function (Fig. 11).

Among these, the biological process category contained the largest number of DEGs, primarily enriched in terms related to sensory perception of chemical stimulus, collagen and cuticulin-based cuticle development, and the defense response. The Cellular Component category ranked second, with major terms including membrane, collagen trimer, and cuticular extracellular matrix. Notably, significant enrichment was observed in membrane-related pathways. Given that membranes are fundamental structural components of cells and serve as a crucial material basis for life activities, these findings suggest that kiwifruit leaf polysaccharides may modulate cell membrane structure and function via multiple molecular targets, thereby influencing cellular development. The Molecular Function category contained the fewest DEGs, with major annotations involving structural constituents of the cuticle, DNA-binding transcription factor activity, and glycosyltransferase activity. Collectively, these results indicate that polysaccharide treatment alters the expression of *C. elegans* genes across diverse functional categories, potentially leading to broad physiological effects.

KEGG pathway enrichment analysis

The functional annotation of the DEGs was conducted via the KEGG database. As shown in Fig. 12A and B, the top 20 enriched pathways were predominantly associated with metabolic pathways, cytochrome P450, histidine metabolism, biosynthesis of unsaturated fatty acids, vitamin digestion and absorption, riboflavin metabolism, pantothenate and CoA biosynthesis, one-carbon pool by



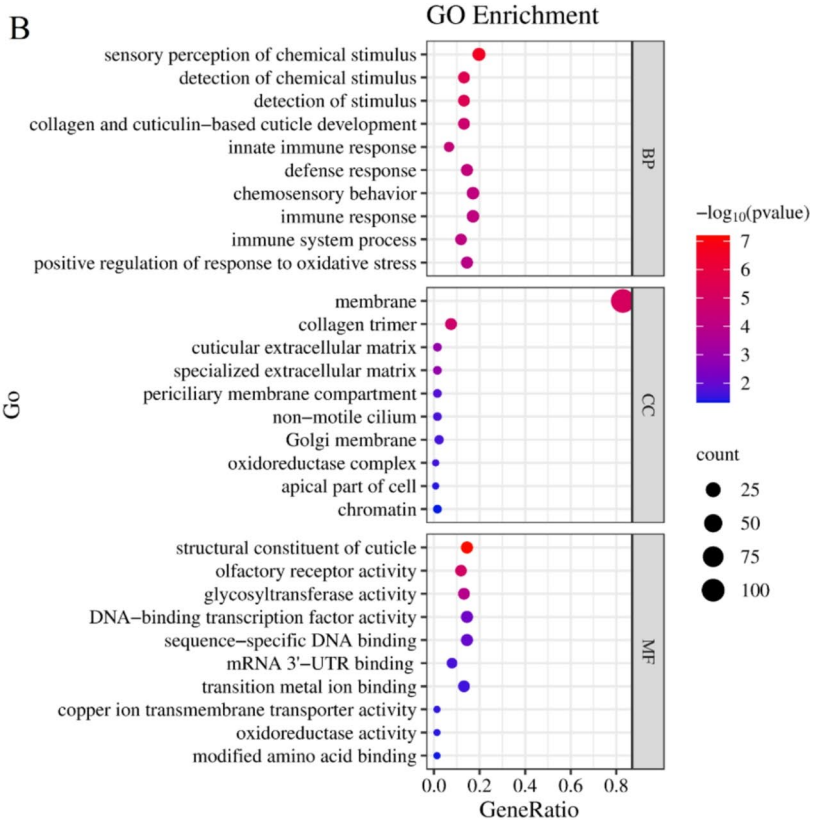


Fig. 11 (**A**) GO annotation analysis plot; (**B**) GO enrichment analysis bubble plot

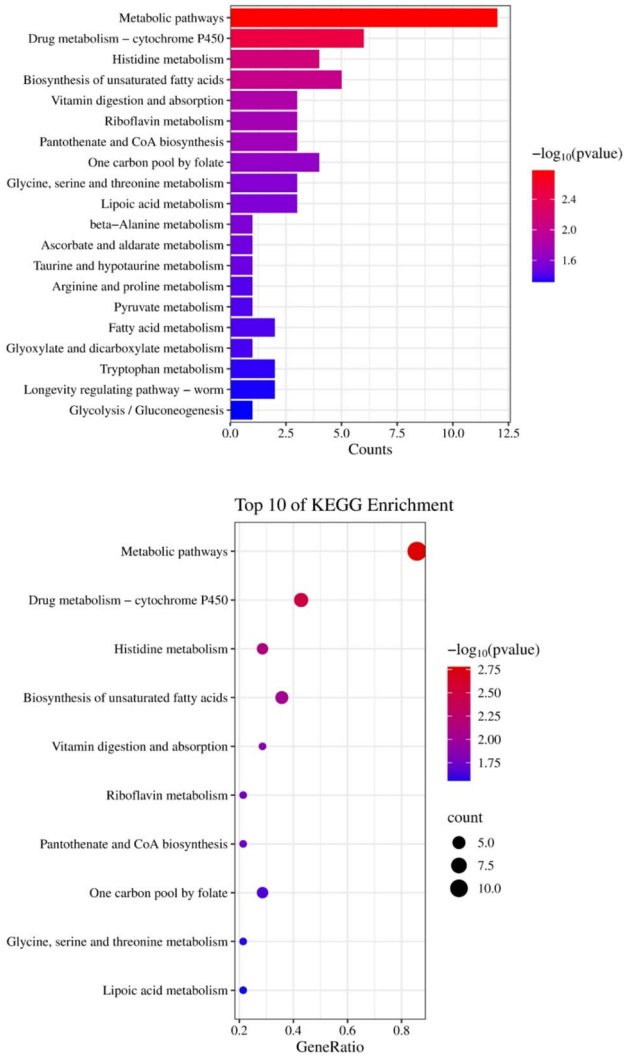


Fig. 12 (**A**) KEGG annotation analysis plot; (**B**) KEGG enrichment analysis bubble plot

folate, and glycine, serine, and threonine metabolism, among others. These results suggest that the anti-aging effects observed in nematodes treated with polysaccharides may be closely linked to the regulation of these metabolic pathways. Recent studies have demonstrated that polysaccharides can delay aging in *C. elegans* by simultaneously modulating multiple biological processes, including lipid metabolism, extracellular matrix homeostasis, and innate immunity. Consistent with these findings, our KEGG enrichment analysis indicated that polysaccharide treatment markedly affected the expression of multiple genes linked to antioxidant defense and aging (Table 6).

In the lipid metabolism pathway, *fat-7* encodes Δ9 fatty acid desaturase, a downstream target of *daf-16*. The enzyme facilitates the desaturation of saturated fatty acids into monounsaturated forms, a metabolic pathway linked to increased lifespan in nematodes [24]. *alh-2* encodes aldehyde dehydrogenase, whose upregulation aids in detoxifying fatty aldehydes generated by oxidative stress, thereby reducing protein damage, maintaining redox homeostasis, and promoting healthy aging [25]. Several upregulated genes (*cyp-14A2*, *cyp-31A2*, *cyp-13A9*, *cyp-29A1*) belong to the cytochrome P450 (CYP) family. These enzymes function as epoxygenases or hydroxylases of long-chain polyunsaturated fatty acids, increasing detoxification and lipid metabolism efficiency and contributing to lifespan regulation [26]. Collagen-encoding genes (*col-138*, *col-63*, *col-38*, *col-175*, *col-49*, *col-137*, *col-110*, *lon-3*, *bli-1*, *and bli-2*) were also significantly affected. These genes are crucial for maintaining extracellular matrix integrity and collagen homeostasis, thereby influencing the growth, development, and motility of nematodes [27]. Within the insulin/IGF-1 signaling (IIS) pathway, *dod-17 and dod-21* enhance innate immune defense, contributing to longevity [28]. *dao-4*, a downstream gene of *daf-2*, is positively regulated by insulin signaling and may also participate in *daf-16*-mediated lifespan extension [29]. The genes K01C8.1 and F08F3.4, which are involved in glycine, serine, and threonine metabolism, generate TCA cycle intermediates, improving energy metabolism and promoting nematode survival [24]. Additionally, *folt-1* and *folt-2* (folate transporter genes) and *gcsh-1* (a core glycine cleavage system gene) participate in glycine metabolism and one-carbon metabolism, increasing NADPH and S-adenosylmethionine production, increasing antioxidant capacity, regulating *daf-16*/FOXO activity, and prolonging lifespan [30]. Interestingly, *fmo-2*, known to promote longevity *via* the tryptophan–one-carbon metabolism pathway under dietary restriction or hypoxic stress, was downregulated under the stable growth conditions of this study. Nevertheless, its associated metabolic pathway may still contribute to lifespan extension [31].

To elucidate interactions among proteins encoded by the differentially expressed genes (DEGs), a protein–protein interaction (PPI) network was constructed via the STRING database (https://string-db.org/) (Fig. 13). The network revealed complex functional associations among these proteins. Key upregulated collagen genes, including *col-49*, *col-38*, and *bli-2*, emerged as central nodes, suggesting that AAP may counteract aging by remodeling the extracellular matrix and maintaining tissue homeostasis. Moreover, the marked upregulation of *dao-4*, which aligns with immune-regulatory pathways, implies its potential role in integrating extracellular matrix regulation with immune homeostasis. Together, the PPI analysis systematically illustrates the functional synergy among the differentially expressed proteins under AAP intervention.

In summary, combined with the DEG, functional enrichment and PPI results, these findings indicate that

Table 6 DEGs related to antioxidation and aging

Functional annotation	Gene ID	Gene Name	Description	P Value	Signal
Lipid metabolism	CELE_F10D2.9	fat-7	Delta(9)-fatty-acid desaturase fat-7	0.0023	up
	CELE_K04F1.15	alh-2	Aldehyde dehydrogenase domain-containing protein	0.0264	up
	CELE_T10B9.6	cyp-13A9	pseudo	0.0238	up
	CELE_C44C10.2	cyp-29A1	pseudo	0.0416	up
	CELE_K09A11.3	cyp-14A2	CYtochrome P450 family	0.0042	up
	CELE_H02I12.8	cyp-31A2	CYtochrome P450 family	0.0444	up
Collagen homeostasis	CELE_Y51H4A.9	col-137	Nematode cuticle collagen N-terminal domain-containing protein	0.0013	up
	CELE_F19C7.7	col-110	Nematode cuticle collagen N-terminal domain-containing protein	0.0026	up
	CELE_K09H9.3	col-49	Cuticle collagen 49	0.0030	up
	CELE_ZK265.2	col-63	Nematode cuticle collagen N-terminal domain-containing protein	0.0053	up
	CELE_W05G11.3	col-88	Nematode cuticle collagen N-terminal domain-containing protein	0.0060	up
	CELE_F54C9.4	col-38	Cuticle collagen 38	0.0064	up
	CELE_C52D10.13	col-138	Nematode cuticle collagen N-terminal domain-containing protein	0.0087	up
	CELE_C35B8.1	col-175	Nematode cuticle collagen N-terminal domain-containing protein	0.0134	up
	CELE_ZK836.1	lon-3	Cuticle collagen lon-3	1.7679E-08	up
	CELE_F59E12.12	bli-2	Nematode cuticle collagen N-terminal domain-containing protein	0.0023	up
	CELE_C09G5.6	bli-1	Cuticle collagen bli-1	0.0067	up
Immune defense	CELE_K10D11.1	dod-17	CUB-like domain-containing protein	0.0004	up
	CELE_C32H11.10	dod-21	CUB-like domain-containing protein	0.0018	up
	CELE_ZC373.6	dao-4	Protein dao-4	0.0036	up
Amino acid metabolism	CELE_D1025.2	gcsh-1	Glycine cleavage system H protein	0.0030	up
	CELE_K01C8.1	srdh-1	L-serine deaminase	0.0445	up
	CELE_F08F3.4	F08F3.4	NAD-dependent epimerase/dehydratase domain-containing protein	0.0026	up
One-carbon metabolism	CELE_K08C7.5	fmo-2	Flavin-containing monooxygenase	0.0118	down
	CELE_F37B4.7	folt-2	Folate-like transporter 2	0.0013	up
	CELE_C06H2.4	folt-1	Folate transporter 1	0.0462	up
Others	CELE_Y45G5AM.1	nhr-114	Nuclear hormone receptor 114	4.8556E-05	up
	CELE_C14C6.4	nhr-155	Nuclear Hormone Receptor family	0.0376	up
	CELE_F15E11.15	pud-3	Upregulated in Daf-2 domain-containing protein	0.0009	up
	CELE_C37A5.2	fipr-22	FIP (Fungus-Induced Protein) Related	0.0241	down
	CELE_C37A5.4	fipr-23	FIP (Fungus-Induced Protein) Related	0.0247	down
	CELE_K06B9.5	pax-2	Paired box protein 2 homolog	0.0355	up

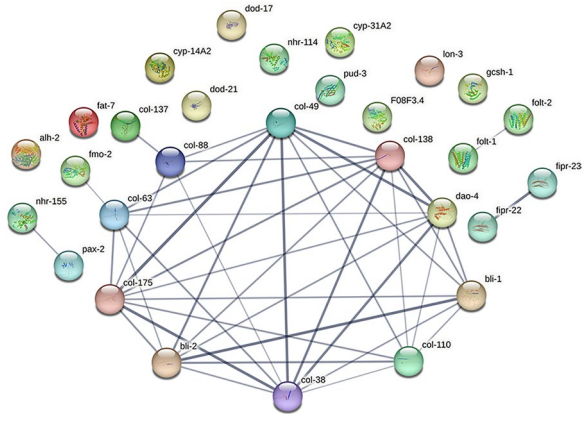


Fig. 13 PPI network interaction diagram

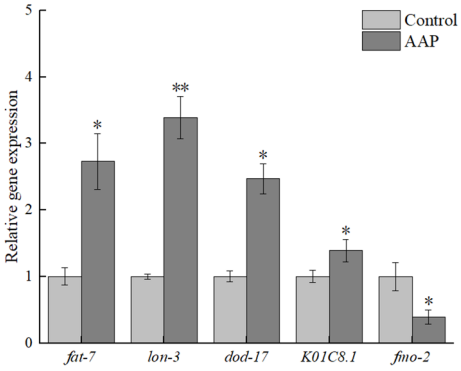


Fig. 14 Validation by qRT–PCR of five differentially expressed genes in *C. elegans* from the control and AAP groups. *act-1* was used as the internal reference gene. ($n = 20$, * $p < 0.05$, ** $p < 0.01$ compared with control nematodes)

polysaccharides may exert antioxidant and anti-aging effects in *C. elegans* via the integrated regulation of multiple molecular targets and signaling pathways.

Validation of the expression of five DEGs via qRT–PCR

On the basis of the significantly differentially expressed genes identified by KEGG pathway enrichment analysis

combined with reports in the anti-aging-related literature [24], this study selected five key differentially expressed genes for verification via qRT−PCR (Fig. 14). *Fat-7* encodes Δ9 fatty acid desaturase, which is involved in lipid metabolism; *lon-3* is involved in the maintenance of collagen homeostasis in nematodes; *dod-17* plays a crucial role in innate immune defense responses; *K01C8.1* participates in regulating the glycine, serine, and threonine metabolism pathways; and *fmo-2* is involved in tryptophan metabolism and one-carbon metabolism pathways. The qRT−PCR results revealed that, compared with those in the control group, the expression levels of *fat-7*, *lon-3*, *dod-17*, and *K01C8.1* in the treatment group were significantly increased ($p < 0.05$), whereas the expression level of *fmo-2* was significantly decreased ($p < 0.05$). This expression trend is consistent with the transcriptome sequencing results, indicating the reliability and reproducibility of the experiment. These results further support that polysaccharides may exert antioxidant and anti-aging effects in nematodes by synergistically regulating multiple pathways, including lipid metabolism (*fat-7*), extracellular matrix homeostasis (*lon-3*), immune defense (*dod-17*), and specific metabolic pathways (*K01C8.1*, *fmo-2*).

Conclusions

This study successfully extracted and purified a pectic polysaccharide (AAP) from *Actinidia arguta* leaves, with comprehensive structural characterization confirming that it is an HG- and RG-I-type pectin. AAP has a unique monosaccharide composition (rhamnose, arabinose, galactose, and galacturonic acid), a weight-average molecular weight of 4.14×10^5 g/mol, and a random coil conformation. The Congo red assay clearly revealed that it lacks a stable triple-helical structure, and these structural characteristics may be closely associated with its biological activity. Functional evaluations in *C. elegans* demonstrated that AAP effectively delays aging by prolonging lifespan, enhancing exercise capacity, and mitigating oxidative damage by reducing lipofuscin and ROS accumulation. Mechanistically, transcriptomic and pathway analyses revealed that AAP acts through a multitarget, multipathway: it regulates lipid metabolism via *fat-7* and cytochrome P450 family genes to maintain fatty acid homeostasis; strengthens extracellular matrix integrity through the upregulation of collagen-encoding genes; enhances innate immunity via insulin/IGF-1 signaling pathway-related genes (*dod-17*, *dod-21*); and modulates amino acid and one-carbon metabolism (via *gcsh-1*, *folt-1/2*) to improve energy metabolism and antioxidant capacity. PPI network analysis further clarified the core role of collagen genes and other genes in anti-aging regulation, and qRT−PCR experiments validated the expression patterns of key DEGs, confirming the reliability of the transcriptomic data. Overall, this research clarifies the structural features of *A. arguta* leaf polysaccharides and their anti-aging mechanism, offering a scientific foundation for the development of AAP as a natural anti-aging ingredient in functional foods or pharmaceutical products. Future studies may focus on optimizing extraction processes and verifying their efficacy in higher organisms to expand their practical applications.

Acknowledgements
This work was supported by the Science and Technology Planning Project of Henan Province (242102311257) and the Major Science and Technology Special Project of Henan Province (231100310200).

Author contributions
Xuewei Jia: Writing-original draft; Investigation; Huijie Xue: Methodology; Investigation; Data curation; Xiao Yang: Methodology; Data curation; Qingdan Yan: Methodology; Yuan Gao: Investigation; Yanchong Qin: Investigation; Tianxiao Li: Methodology; Project administration; Jun Hu: Methodology; Supervision; Writing-review & editing; Chunping Xu: Writing-review & editing; Project administration. The authors have accepted responsibility for the entire content of this manuscript and approved its submission.

Funding
This work was supported by the Science and Technology Planning Project of Henan Province (242102311257) and the Major Science and Technology Special Project of Henan Province (231100310200).

Data availability
Data are available upon reasonable request to the corresponding authors.

Declarations

Competing interests
The authors declare that they have no known competing financial interests or personal relationships that could have appeared to influence the work reported in this paper.

Received: 5 September 2025 / Accepted: 27 December 2025
Published online: 05 February 2026

References

1. Zhang H, Teng K, Zang H (2023) Actinidia Arguta (Sieb. Et Zucc.) Planch. Ex Miq.: a review of phytochemistry and pharmacology. Molecules 28:7820. https://doi.org/10.3390/molecules28237820
2. Pinto D, Delerue-Matos C, Rodrigues F (2020) Bioactivity, phytochemical profile and pro-healthy properties of *Actinidia arguta*: a review. Food Res Int 136:109449. https://doi.org/10.1016/j.foodres.2020.109449
3. Silva AM, Luis AS, Moreira MM, Ferraz R, Brezo-Borjan T, Svarc-Gajic J, Costa PC, Delerue-Matos C, Rodrigues F (2022) Influence of temperature on the subcritical water extraction of *Actinidia arguta* leaves: a screening of pro-healthy compounds. Sustain Chem Pharm 25:100593. https://doi.org/10.1016/j.scp.2021.100593
4. Kim GD, Lee JY, Auh JH (2019) Metabolomic screening of anti-inflammatory compounds from the leaves of *Actinidia arguta* (Hardy Kiwi). Foods 8:47. https://doi.org/10.3390/foods8020047
5. Almeida D, Pinto D, Santos J, Vinha AF, Palmeira J, Ferreira HN, Rodrigues F, Oliveira MBPP (2018) Hardy kiwifruit leaves (*Actinidia arguta*): an extraordinary source of value-added compounds for food industry. Food Chem 259:113–121. https://doi.org/10.1016/j.foodchem.2018.03.113
6. Hou Y, Bai L, Wang X, Zhang S, Liu S, Hu J, Gao J, Guo S, Ho C, Bai N (2023) Gut microbiota combined with serum metabolomics to investigate the

hypoglycemic effect of *Actinidia arguta* leaves. Nutrients 15:4115. https://doi.org/10.3390/nu15194115
7. Cao M, Zheng J, Zhang Y, Li F, Rui Y, Jian Z, Zhao F, Tao A (2025) *Actinidia* polysaccharides: a potential bioactive substance-extraction, structure, and bioactivity studies. Int J Biol Macromol 311:144012. https://doi.org/10.1016/j.ijbiomac.2025.144012
8. Jia X, Liu Y, Chen Z, Li T, Lu C, Xu C (2025) Impact of molecular weight and chain rigidity on the endocytosis and anti-tumor activity of seleno-lentinan. J Future Foods 5:419–427. https://doi.org/10.1016/j.jfutfo.2024.07.020
9. Yu G, Liu Y, Gao Y, Jia X, Ma R, Li T, Feng W, Xu C (2025) Structure characterization and antioxidant properties of a triple helix galactoglucomannan from the fruiting bodies of *Russula virescens* (Agaricomycetes). Int J Med Mushrooms 27:45–56. https://doi.org/10.1615/IntJMedMushrooms.2024057484
10. Yu Y, Duan Y, Ma S, Hu Q, Ma G (2025) Research progress on the mechanism of functional activity of edible fungi polysaccharides—focusing intestinal mucus as a key and entry point. Food & Medicine Homology 2:9420042. https://doi.org/10.26599/FMH.2025.9420042
11. Jiang W, Hu Y, Zhu Z (2025) Optimization of extraction process and evaluation of biological activities of polysaccharides from Zingiber striolatum. J Light Ind 40:10–19. https://doi.org/10.12187/2025.04.002
12. Guo X, Luo J, Qi J, Zhao X, An P, Luo Y, Wang G (2022) The role and mechanism of polysaccharides in anti-aging. Nutrients 14:5330. https://doi.org/10.3390/nu14245330
13. Yan JK, Wang C, Chen TT, Li L, Liu X, Li L (2023) Structural characteristics and ameliorative effect of a polysaccharide from corbicula fluminea industrial distillate against acute liver injury induced by CCl(4) in mice. Int J Biol Macromol 227:391–404. https://doi.org/10.1016/j.ijbiomac.2022.12.138
14. Jia X, Wang X, Liu Y, Sun Y, Ma B, Li Z, Xu C (2021) Structural characterization of an alkali-extracted polysaccharide from *Dioscorea opposita* Thunb. with initial studies on its anti-inflammatory activity. J Carbohydr Chem 40:308–324. https://doi.org/10.1080/07328303.2021.2009503
15. Yu B, Zhang D, Wu Y, Tao W, Luorong Q, Luo J, Tan L, Chen H, Cao W (2023) A new polysaccharide from Hawk tea: structural characterization and immunomodulatory activity associated with regulating gut microbiota. Food Chem 418:135917. https://doi.org/10.1016/j.foodchem.2023.135917
16. Vityazev FV, Golovchenko VV, Patova OA, Khlopin VA, Kosolapova NV, Dmitrenok AS, Shashkov AS (2024) Pectic polysaccharides of black radish taproots: extraction, structural characterization. Food Chem 436:137692. https://doi.org/10.1016/j.foodchem.2023.137692
17. Liu L, Sui Y, Wang T, Li X, Chen L, Shi M (2024) Physicochemical and antioxidant properties of pectin from *Actinidia arguta* Sieb.et Zucc (*A. arguta*) extracted by ultrasonic. Front Nutr 11:1349162. https://doi.org/10.3389/fnut.2024.1349162
18. Jia X, Wu Y, Liu Z, Dai Y, Li T, Gao M, Xu C (2024) Coating effect of renatured triple-helix lentinan on the morphology and antimicrobial activity of ZnO synthesized by hydrothermal method. RSC Adv 14:17814–17823. https://doi.org/10.1039/d4ra01590h
19. Liu N, Zou S, Xie C, Meng Y, Xu X (2023) Effect of the β-glucan from *Lentinus edodes* on colitis-associated colorectal cancer and gut microbiota. Carbohydr Polym 316:121069. https://doi.org/10.1016/j.carbpol.2023.121069
20. Liu D, Tang W, Huang XJ, Hu J, Wang J, Yin J, Nie S, Xie M (2022) Structural characteristic of pectin-glucuronoxylan complex from *Dolichos lablab* L. hull. Carbohydr Polym 298:120023. https://doi.org/10.1016/j.carbpol.2022.120023
21. Huamani-Palomino RG, M PR, Oliveira G, Kock FVC, Venâncio T, Córdova BM (2023) Structural elucidation of pectin extracted from cocoa pod husk (*Theobroma Cacao* L.): evaluation of the degree of esterification using FT-IR and 1H NMR. Biomass Convers Biorefin 15:2047–2061. https://doi.org/10.1007/s13399-023-04082-3
22. Liu Y, Odiba AS, Yu Q, Xie J, Okoro NO, Liao G, Zhu X, He B, Jin C, Fang W, Wang B (2025) Alkaloids extracted from dendrobium officinale grown in diverse environments exhibited robust antioxidative and anti-aging activity. J Future Foods 5:591–604. https://doi.org/10.1016/j.jfutfo.2024.11.007
23. Hou Z, Xia Y, Sun Y, Yang M, Wang L, Xu W, Zhao X (2025) Sodium alginate-based photothermal film: Preparation, antibacterial activity, and application for preservation of Kyoho grapes. https://doi.org/10.1016/j.jfutfo.2024.10.004. J Future Foods
24. Sun J, Zhong X, Sun D, Xu L, Shi L, Sui J, Liu Y (2023) Anti-aging effects of polysaccharides from ginseng extract residues in *Caenorhabditis elegans*. Int J Biol Macromol 225:1072–1084. https://doi.org/10.1016/j.ijbiomac.2022.11.168
25. Zeng L, Li X, Preusch CB, He GJ, Xu NY, Cheung TH, Qu JA, Mak HY (2021) Nuclear receptors NHR-49 and NHR-79 promote peroxisome proliferation to compensate for aldehyde dehydrogenase deficiency in *C. elegans*. PLoS Genet 17:e1009635. https://doi.org/10.1371/journal.pgen.1009635
26. Larigot L, Mansuy D, Borowski I, Coumoul X, Dairou J (2022) Cytochromes P450 of *Caenorhabditis elegans*: implication in biological functions and metabolism of xenobiotics. Biomolecules 12:342. https://doi.org/10.3390/biom12030342
27. Zhu Y, Li W, Dong Y, Xia C, Fu R (2023) *C. elegans* hemidesmosomes sense collagen damage to trigger innate immune response in the epidermis. Cells 12:2223. https://doi.org/10.3390/cells12182223
28. Liu D, Pei H, Yao K, Gao J, Chen H, Tong P (2025) Ovalbumin alters DAF-16 class-II/I gene expressions *via* insulin/insulin-like growth factor-1 signaling to initiate the innate immune response of *Caenorhabditis elegans*. Mol Immunol 179:116–127. https://doi.org/10.1016/j.molimm.2025.02.007
29. Pei H, Lin Z, Yao K, Luo Y, Tong P, Chen H, Wu Y, Wu Z, Gao J (2024) Ovalbumin promotes innate immune response of *Caenorhabditis elegans* through DAF-16 and SKN-1 pathways in insulin/IGF-1 signaling. J Physiol Biochem 80:541–559. https://doi.org/10.1007/s13105-024-01021-2
30. Liu YJ, Janssens GE, McIntyre RL, Molenaars M, Kamble R, Gao AW, Jongejan A, van Weeghel M, MacInnes AW, Houtkooper RH (2019) Glycine promotes longevity in *Caenorhabditis elegans* in a methionine cycle-dependent fashion. PLoS Genet 15:e1007633. https://doi.org/10.1371/journal.pgen.1007633
31. Choi HS, Bhat A, Howington MB, Schaller ML, Cox RL, Huang S, Beydoun S, Miller HA, Tuckowski AM, Mecano J, Dean ES, Jensen L, Beard DA, Evans CR, Leiser SF (2023) FMO rewires metabolism to promote longevity through tryptophan and one carbon metabolism in *C. elegans*. Nat Commun 14:62. https://doi.org/10.1038/s41467-023-36181-0

Publisher's note

Springer Nature remains neutral with regard to jurisdictional claims in published maps and institutional affiliations.